



Production of acrylic acid from Bio-Derived lactic acid over a Defect-Rich molybdenum phosphosulfide catalyst



Neha Dhiman^{a,b}, Sudhakara Reddy Yenumala^{b,c}, Deepti Agrawal^{b,d}, Ankit Pandey^e, Jyoti Porwal^d, Bipul Sarkar^{a,b,*}

^a Catalytic De-Polymerization Area, Upstream & Wax Rheology Division, CSIR-Indian Institute of Petroleum, Dehradun 248005, India

^b Academy of Scientific and Innovative Research (AcSIR), CSIR-HRDC Campus, Joggers Road, Kamla Nehru Nagar, Ghaziabad 201 002, India

^c Thermo-catalytic Processes Area, Material Resource Efficiency Division, CSIR-Indian Institute of Petroleum, Dehradun 248005, India

^d Biochemistry and Biotechnology Area, Material Resource Efficiency Division, CSIR-Indian Institute of Petroleum, Dehradun 248005, India

^e Nano Catalysis Area, Light Stock Processing Division, CSIR-Indian Institute of Petroleum, Dehradun 248005, India

ARTICLE INFO

Keywords:

Dehydration
Defect-rich catalyst
Acrylic Acid
Lactic acid

ABSTRACT

Introducing phosphorous and sulphur with molybdenum possess molybdenum phosphosulfate (MoP|S), and the material showed significant activity and stability for the vapour phase dehydration of bio-derived lactic acid to acrylic acid. Adding excessive thiourea-raptured layer spacing creates a defect-rich catalytic structure with more edges and kinks. This disordered atomic arrangement on the basal surface enhanced the dehydration performances of MoS_2 catalysts. Considering the inverse trend of acetaldehyde and AA selectivity, we can assume that the decarboxylation of LA is favoured at low temperatures, whereas dehydration is favoured at high temperatures. Rate expression governed by the power law equation was found to be the best fit during the kinetic study, and the E_a of the dehydration was 11.39 KJ/mol. A conversion of 94% with a selectivity of 91% for acrylic acid at 450 °C was achieved over the defect-rich MoS_2 catalyst.

1. Introduction

The modern production of fuels and chemicals is mainly based on crude oil refining. However, it is essential to incorporate renewable resources along with traditional feedstock to achieve sustainable development [1–5]. The industry has devoted tremendous efforts to attain sustainability, but plastics (or polymers) are mainly manufactured with fossil resources. Meanwhile, new research initiatives offer various processes to produce bio-based polymers and monomers. That would reduce the dependency on fossil-based fuels, and consumer goods can help achieve the targeted net reduction in CO_2 emissions by 55% by 2030 in European Union countries [6]. Thus, utilising bio-based sustainable feedstock to synthesise fine chemicals is of the utmost importance [7]. Much research on bio-renewable feedstock has been described to decrease the need for fossil fuels, particularly petroleum. In retrospect, the opportunity for fermentation-based chemicals shall boost new value chains with bio-based feedstock as the starting point and bio-refineries at the core.

Acrylic acid is an essential industrial monomer used to form acrylate polymers in superabsorbent polymers and adhesives [8–10]. Global

acrylic acid demand was 5750 KT in 2014 and is expected to reach 8750 KT by 2022, growing at a CAGR of 5.6% [11]. Partial oxygenation of propene remains the predominant source of acrylic acid and depends heavily on processing petrochemicals as the base raw material. The purpose of this practice is to produce acrylic acid from (a) renewable carbon sources and (b) value addition of fragmentation products (such as raw lactic acid) in a sustainable manner. Among the alternate production of acrylic acid, the aldol condensation of acetic acid with formaldehyde [12–14], glycerol to acrylic acid via acrolein has attracted much research attention. The catalytic dehydration of lactic acid from the bio-genic route is considered an alternative green process for the production of acrylic acid pertaining to the bio-refining concept [15]. Lactic acid (LA) is a promising renewable feedstock attained by biomass fermentation that may have a vital role in upcoming bio-refineries [16]. It can be converted to several high-value chemicals other than acrylic acid, such as acetaldehyde, pyruvic acid, 2,3-pentanedione, 1,2-propandiol and lactic esters. Among them, acetaldehyde produced through decarboxylation of lactic acid is considered the major side product responsible for low acrylic acid selectivity [15].

The most challenging part is, without any doubt, the design of new

* Corresponding author at: Catalytic De-Polymerization Area, Upstream & Wax Rheology Division, CSIR-Indian Institute of Petroleum, Dehradun 248005, India.
E-mail address: bsarkar@iip.res.in (B. Sarkar).

catalytic materials for selective dehydration reactions. Numerous catalysts with appropriate acid-base properties have been reported for the selective dehydration of lactic acid. Primarily, metal phosphates [15,17], sulphates [18], and modified zeolites [10,15,19,20] were extensively reported in the gas phase dehydration of lactic acid. Alkali-modified catalyst route the reaction through the formation of alkali lactate by interacting with the metal cations. This formation of alkali lactate appeared to be critical in the formation of acrylic acid selectively [21]. Shi et al. have tried to improve the performances NaY by adding potassium, i.e., KNaY, at an optimised reaction temperature between 280 and 370 °C [21]. The addition of potassium substantially increased the yield of acrylic acid to 37.3% from 28.5% over NaY, at 340 °C. Further, by modifying the NaY with lanthanides (La, Ce, Sm and Eu), Huang et al. found total lactic acid conversion with 56% acrylic acid selectivity with 2 %LA/NaY catalyst [22]. Rapid catalyst deactivation was observed despite these findings, even in short-term runs and more selective catalysts.

Secondly, all the studies have been conducted with the commercial and pure lactic acid (AR/LR) solution in water. No study has ever been documented in which real-time lactic acid fermentation broth derived from lignocellulosic sugars has been valorised to acrylic acid using a chemo-catalytic route. Indeed, the development of biorefinery processes requires studies with real-time feedstocks, and that would be one of the major prerequisites for establishing an economy based on bio-resources. In the present work, a molybdenum phosphosulfate (MoP|S) based catalyst was synthesised and used for transforming lactic acid into acrylic acid. Lactic acid was produced through a fermentative pathway using glucose-rich enzymatic hydrolysates derived from alkali pretreated sugarcane bagasse (SCB). The unique MoP|S catalyst has a complete morphology, high crystallinity, and acidity. This study could help to understand the potential of fermentative won lactic acid as the feedstock for bio-acrylic acid production and develop more efficient solid catalysts for potential bio-refining intervention.

2. Experimental

2.1. Feedstock

L (+) lactic acid was produced using a homo-fermentative and thermophilic *Bacillus coagulans* NCIM 5648, purchased from the National Collection of Industrial Microorganisms (NCIM), Pune, India. High-solids enzymatic saccharification of alkali pretreated SCB was performed using Cellic CTec2 using an optimised strategy [23]. Later, sugar-rich enzymatic hydrolysate (≥ 165 g/L glucose and xylose) was valorised to L(+)lactic acid using *B. coagulans* NCIM 5648 under pH-controlled conditions, as described earlier [24]. When the glucose in the broth was completely exhausted, the fermentation was terminated. Cell-free, the lactic acid-rich broth was obtained by centrifugation at 7500 rpm for 10 min at 4 °C. This SCB-derived lactic acid served as the starting feedstock for bio-acrylic acid production. The broth was suitably diluted to carry out dehydration trials.

2.2. Materials

Ammonium molybdate tetrahydrate ($(\text{NH}_4)_6\text{Mo}_7\text{O}_{24} \cdot 4\text{H}_2\text{O}$) and Orthophosphoric acid (H_3PO_4 , 88%) were purchased from TCI chemicals and Across chemicals, respectively. Acrylic acid (99.9%), Propanoic acid (99%), acetaldehyde (98%), and Acetic acid (98%) were obtained from Sigma-Aldrich. All the chemicals were used without further purification; double distilled water was obtained using a Borsil® unit installed in the laboratory.

2.3. Catalyst preparation

10 g ammonium molybdate tetrahydrate ($(\text{NH}_4)_6\text{Mo}_7\text{O}_{24} \cdot 4\text{H}_2\text{O}$) was first dissolved in 100 ml of distilled water under stirring at 85 °C for 1 h.

An aqueous solution of orthophosphoric acid (2 wt%, i.e., 0.332 g of 88% H_3PO_4 ; into 30 ml distilled water) was added dropwise, then thiourea (NH_2CSNH_2) solution (6 g in 80 ml water) was added to the mixture. The mixture was kept under stirring at 85 °C. After 30 min, the resulting homogenous solution was transferred into a Teflon-lined stainless-steel autoclave for hydrothermal treatment at 180 °C for 24 h under autogenous pressure. The obtained material was filtered and washed with distilled water several times. The mixture was kept at 80 °C overnight in an oven and then dried. The dried sample was calcined at 450 °C for 6 h. The final product was coded as $\text{MoP}_{(\text{wt}\%)}|\text{S}$ catalyst. All reference catalysts were coded as (wt%)M/zeolite or (wt%) M_1 (wt%) M_2 /zeolite where M_1 and M_2 refers to 1st and 2nd metal respectively.

2.4. Catalyst screening

The dehydration reaction of bio-derived lactic acid (LA) to acrylic acid was carried out in a fixed-bed flow quartz reactor of 8.5 mm inner diameter under atmospheric pressure. 1 g palletised catalyst with 30–40 mesh was placed in the middle of the reactor. Silicon carbide was used to fill above and below the catalyst bed. The reactor was placed in the middle of a furnace and heated to the reaction temperature of 350 °C. The catalyst was pretreated at the reaction temperature (350–475 °C) for 1 hr under high purity N_2 atmosphere (flow rate = 16 ml/min). Then, the reaction feed (~20 wt% of LA in water) was pumped into the reactor ($\text{LHSV} = 2\text{--}6 \text{ h}^{-1}$), along with 16 ml/min nitrogen flow. The reaction temperature for lactic acid dehydration was examined in the range of 350–475 °C. The reaction product was condensed and analysed by high-performance liquid chromatography (HPLC) equipped with an Amine-X-HPX-87H column. Conversion and selectivity were calculated according to the following equations.

$$C_{\text{LA}}(\%) = \frac{F_{\text{LA}, \text{in}} - F_{\text{LA}, \text{out}}}{F_{\text{LA}, \text{in}}} \times 100\%$$

$$S_{\text{AA}}(\%) = \frac{F_{\text{AA}, \text{out}}}{F_{\text{LA}, \text{in}} - F_{\text{LA}, \text{out}}} \times 100\%$$

$$Y_{\text{AA}} = \frac{F_{\text{AA}, \text{out}}}{F_{\text{LA}, \text{in}}} \times 100$$

2.5. Characterisations

Powder X-ray Diffraction (XRD) patterns were carried out on a Bruker D8Advance X-ray diffractometer with $\text{Cu K}\alpha$ ($\lambda = 1.5418 \text{ \AA}$) monochromatic radiation having the 2θ range from 2 to 80° with step size 0.04°. The FEI Quanta 200F Scanning Electron Microscope (SEM) system was equipped with energy-dispersive X-ray spectroscopy (EDX) to obtain the catalyst's morphological information and elemental maps. The Transmission Electron microscopy (TEM) analyses were carried out using a JEM-2010 instrument (JEOL, Japan). The accelerating voltage turned into two hundred kV, and the decision turned into 1.4 Å. The samples have been loaded on a Lacey Formvar/ carbon-lined copper grid through dispersion in ethyl alcohol using an ultrasonic processor. TriStar 3000 (Microsoft Corp) was used for N2 adsorption-desorption analysis for specific surface properties and catalyst pore volume. Before analysis, the sample was vacuum treated at 120 °C for 12 h. The elemental composition and the oxidation state of the catalysts were determined by X-ray photoelectron spectroscopy (Kalpha, Thermo Scientific Corp). Binding energies were normalised concerning the position of the C 1 s peak at 284.5 eV. The pyridine-adsorbed FT-IR (Py-IR) spectrum was obtained on a Nicolet FTIR spectrometer. Before analysing, pyridine was adsorbed on samples, and the mixture was kept at room temperature overnight in the air. Then samples were kept in the oven at 100 °C for 1 h. The prepared sample was grounded with potassium bromide, made pellets using the hydraulic press, and analysed. Ammonia temperature-programmed desorption (NH₃-TPD) experiments

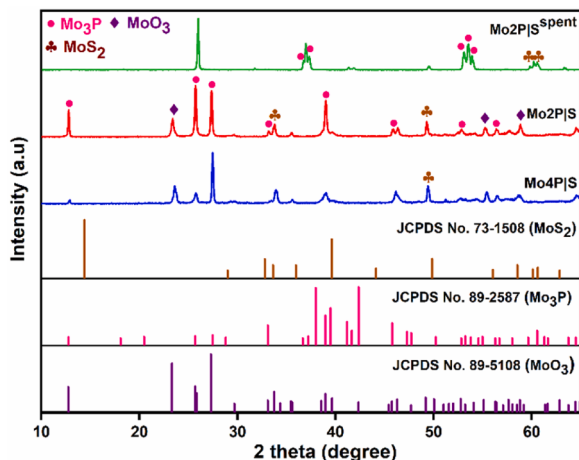


Fig. 1. XRD patterns for different MoP|S catalysts along with the standard XRD data of MoS₂, Mo₃P and MoO₃.

were recorded on Micromeritics, Auto Chem II 2920 instrument by thermal conductivity detector (TCD). Thermogravimetric analyses were carried out with the Perkin-Elmer diamond analyser. The thermal stability of samples (fresh and spent) was heated in flowing air after 60 to 900 °C at a 5 °C/min heating rate. A Bruker AV III instrument is used to perform solid-state ³¹P NMR 500 MHz organised with MAS (4 mm)

probe. Before analysis, the sample was dried, ground (with mortar-pestle), and tightly packed into a zirconium rotor. Raman experiments were carried out using a Horiba Jobin Yvon HR 800UV instrument using a 632.8 nm (wavelength, λ L) laser.

3. Results and discussion

The powder X-ray diffractogram (XRD) of different Mo catalysts and references are shown in Fig. 1a. All the Mo samples display sharp peaks, are representative of good crystallinity, and match well with the standard Mo₃P (JCPDS card: 89–2587) and MoS₂(JCPDS card: 73–1508) phases. The coexistence of both the Mo₃P& MoS₂ phase becomes increasingly evident in the formation of MoP|S [25]. Moreover, the presence of the MoO₃ phase (JCPDS card: 89–5108) indicates the presence of scattered formation oxide of molybdenum beside MoP|S.

The XRD pattern of fresh Mo2P|S displays peaks at 20 12.8, 25.6, 27.4, 33.8, 39.0, 45.8, 52.9 and 56.5° correspond to (110), (220), (211), (301), (112), (222), (440) and (600) planes of Mo₃P (JCPDS card: 89–2587). The scattered peak at 33.8 and 49.3° corresponds to (101) and (105) planes of MoS₂, which is in accordance with the JCPDS card no 73–1508 & 37–1492. The peak at 23.4 °C (110) suggests the coexistence of MoO₃ in both the MoP|S. New peaks for Mo₂P in the region of 36.7–37.2 and 53.1–54.0, along with the peaks for MoS₂ at 59.8–60.5 °C, appears in the spent catalyst. The disappearance of peaks at 23.4, 27.4 and 39.0° can be associated with the sintering of the spent catalyst. At the same time, the relative intensity of the spent catalyst

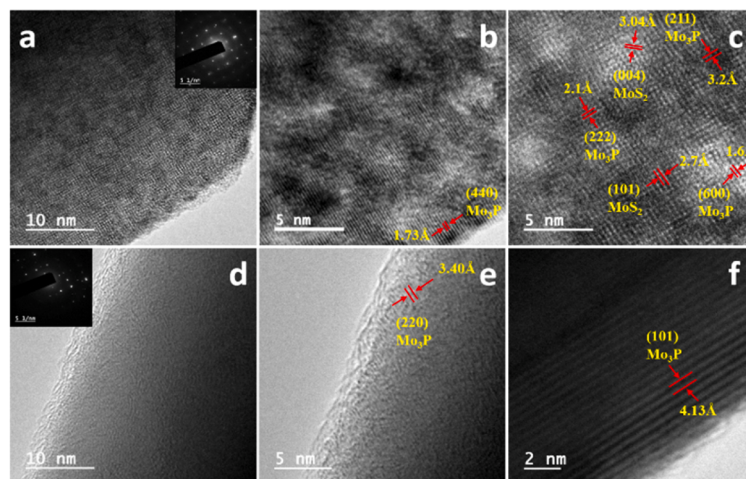


Fig. 2. TEM images of (a-c) fresh and (d-f) spent Mo₂P|S catalysts.

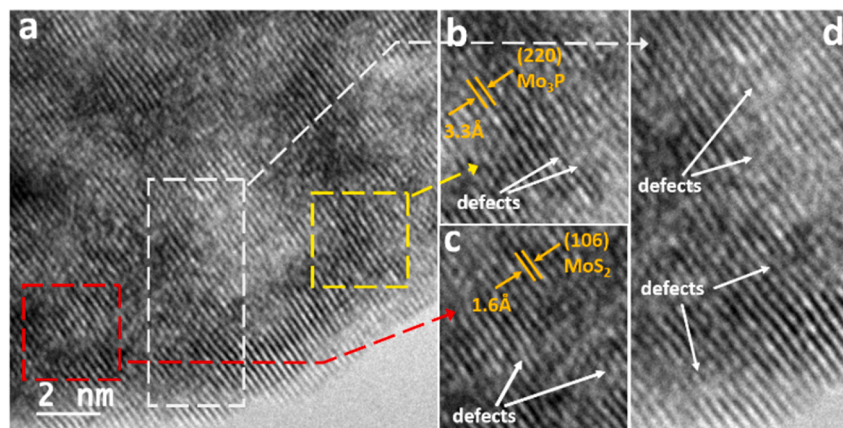


Fig. 3. (a) TEM images of the defect-rich Mo₂P|S nanosheets. (b-d) HRTEM image and the corresponding Fourier transform patterns of boxed areas in the image (a).

Table 1Surface Area, NH₃ Uptake, and Total Acidity of Mo Catalysts.

Catalyst	S _{BET} (m ² /g)	Pore Size (nm)	Pore Volume (cm ³ /g)	B/L Ratio	Total acidity (mmol/g) ^b
MoO ₃	0.18	20.39	0.003	1.14	0.097
MoS ₂	9.46	23.34	0.047	–	–
Mo ₃ P	47.80	3.54	0.039	–	–
Mo2P S	10.74	22.37	0.058	1.44	0.313
Mo2P S ^{spent}	2.95	22.83	0.012	–	0.114
Mo4P S	0.06	–	–	1.56	0.073

The spent catalyst was recovered after 3 h time on steam. ^a B/L ratio ^b Total acidity observed by NH₃-TPD technique.

suggests no loss of crystallinity during the reaction.

The FESEM images of the MoP|S catalyst (Figure S1) clearly reveal the large nanosheets aggregated to form flack-type morphology. The horizontal size of the nanosheets is in the range of 60–100 nm, where straight and wavy shapes can be observed. The TEM images of MoS₂, MoP and MoP|S catalysts are shown in Fig. 2& S2. The TEM reveals that MoP|S catalyst has an assembly of nanoflakes with hierarchical microstructures in it. The average crystallite size was calculated using the full width at half maximum (FWHM) of the (222) diffraction patterns using the Scherrer equation (detailed in supporting information). The average particle size was found between 29 and 21 nm (Table S1), where the thickness of the nanosheet was 5.0 nm with respect to the lattice fringes

corresponding to P-Mo-P.

The HRTEM images of Mo2P|S catalyst top views are shown in Fig. 3; the lattice fringes corresponding to Mo₃P and MoS₂ can be observed from the top-view image. It is worth observing that some of the layer spacing was ruptured. Investigating the HRTEM images in Fig. 3 reveals the directions of (220) and (106) planes of Mo₃P and MoS₂ on the basal surface are not identical. Actually, in some of the places (in Fig. 3b-d), it shows slightly twisted from each other portentous disordered atomic arrangement on the basal surface [26]. These distorted and dislocated sites suggest a novel defect-rich catalytic structure and can also be accredited to the rich defects sites (indexed in Fig. 3b-d) [26]. As a result, the defect-rich structure leads to additional active sites for dehydration activity (discussed later). The spent MoP|S catalyst shows foggy black images appearing due to the deposition of amorphous carbon, which agrees with the Raman data. The EDS elemental mapping evidenced an overall homogeneous presence of S and P in MoP|S (Figure S3).

The adsorption-desorption isotherm (S_{BET}) of fresh and spent Mo2P|S catalyst is shown in Figure S4. All the samples show type III isotherm with moderate P/P₀ values hysteresis loop (H3 type, as identified by IUPAC). The Mo2P|S catalyst shows a reasonably good surface area (S_{BET} = 10.7 m² g⁻¹) in comparison to the surface area of as-synthesised molybdenum oxide, sulphide, and phosphate (in Table 1). Although, the S_{BET} was noted to decrease with the loading of phosphorus (Table 1), which might be caused by the pore covering with metal loading. For the spent catalyst, the reduced surface area may be caused by the adsorption of water during the reaction. Moreover, the pore volume also increased

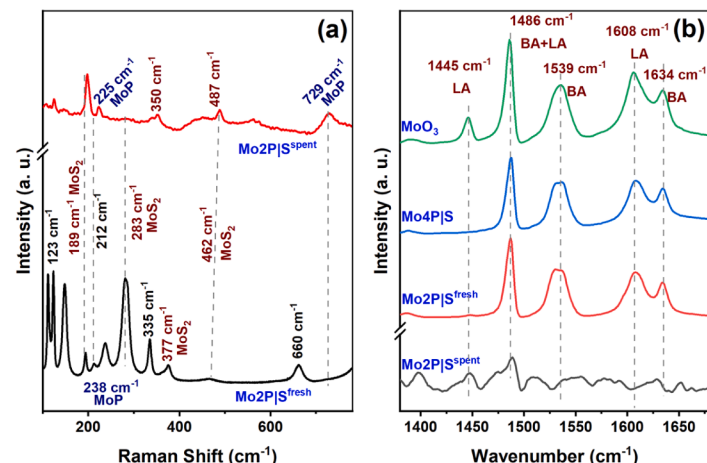


Fig. 4. (a) Raman spectra of fresh and spent Mo2P|S catalyst and XPS spectra of (a) Mo 3d; (b) S 2p (c) P 2p. Note- (spent catalyst; recovered after 6 h time-on-steam) and (b) Pyridine adsorb FTIR of different catalyst.

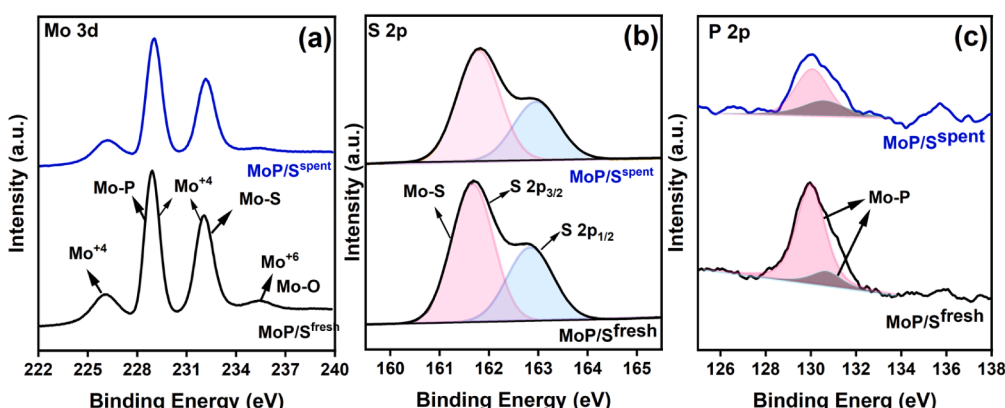
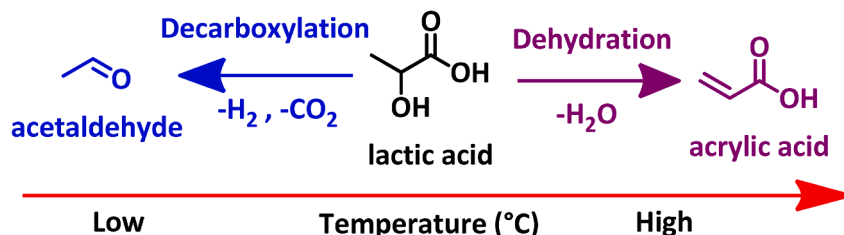


Fig. 5. XP spectra of Mo 3d, S 2p and P 2p of MoP|S catalyst.



Scheme 1. General pathway for lactic acid dehydration and decarboxylation to acrylic acid and acetaldehyde.

because of the pore soiling by the water vapour.

Fig. 4a shows Raman spectra of fresh and spent Mo2P|S catalyst; the Raman shifts at 189, 283, 377 and 462 cm^{-1} correspond to the MoS_2 of symmetries $\text{A}1\text{g}(\text{M})$ - $\text{LA}(\text{M})$, $\text{E}1\text{g}(\Gamma)$, $\text{E}2\text{g}(\Gamma)$ and $\text{A}2\text{u}(\Gamma)$ nodes [27]. The nodes at 238 and 377 cm^{-1} relate to the MoP of various Mo-P-O systems in a structural model [28]. The orthorhombic phase of $\alpha\text{-MoO}_3$ is also observed alongside the MoS_2 and MoP at 225, 660, 818 and 992 cm^{-1} [29]. These characteristic bands are accredited to the eight Raman active modes of orthorhombic $\alpha\text{-MoO}_3$ of symmetries $\text{A}2\text{g}$, $\text{B}2\text{g}$ & $\text{B}3\text{g}$, Ag & $\text{B}1\text{g}$ and Ag & $\text{B}1\text{g}$ modes, respectively [30].

The XP spectra of the fresh MoP|S catalyst specified the existence of Mo in mixed composition, i.e., MoP and MoS₂. The unfolded spectra of the Mo 3d region exposed as the predominant peak at 226.2, 228.9 and 232.4 eV are assigned to Mo⁺⁴. The other peak at 235.6 eV indicates the presence of Mo⁺⁶. Two peaks at 228.9 and 232.4 eV generally correspond to Mo-P and MoS₂ in the MoP|S catalyst [25,31–33]. Besides the Mo⁺⁴ 3d_{5/2} signal, a small peak at 226.4 eV resulted from S 2 s orbital [32]. The peaks at 235.4 eV (Mo⁺⁶) can be assigned to the isolated presence of MoO₃ (which is supported by XANES) [33]. The presence of oxidised moieties is due to the storage problem of the sample, which partially oxidised the sample to MoO₃. Overall, peak intensity is significantly reduced due to coke deposition. XP spectra also revealed the presence of sulphur at the surface using the S 2p_{3/2} peak, which can be resolved into two distinct peaks at 161.6 and 162.8 eV. The corresponding peaks originate from the Mo-bound sulphide species (S²⁻) in molybdenum sulphide (MoS₂) [32]. The P 2p (Fig. 5c) spectra were deconvoluted into two peaks. The prominent peak was observed at 129.8 and 130.6 eV, which are assigned to the low valence P in MoP [33].

We also performed a XANES study to elucidate the origin of MoO₃; from the data, we could understand the nature of the molecular composition in MoP|S. During the analysis, we took extreme precautions to avoid material oxidation. Figure S5 shows the XANES pattern of MoO₃ foil, fresh and spent MoP|S catalyst. The Mo-K-edge spectra with peaks at 20000–20020, 20015 and 20030 eV represent the presence of MoS₂, Mo₃P and MoO₃, respectively [34–36]. In the MoP|S catalyst, the signatures for MoS₂ and Mo₃P are visible at BE 20000–20020 eV, while the peak for MoO₃ at 20030 eV is not visible. This observation indirectly supports the partial oxidation of the catalyst in the air atmosphere, where the oxides of Mo are present in trace amounts.

3.1. Nature of acidity (Py-IR)

NH_3 -TPD in Figure S6 shows a significant amount of NH_3 ware desorbed between 170 and 270 °C. The plot of temperature Vs. TCD signal exhibited weak acidic sites at 109 and 146 °C, whereas the signal at 229 °C was ascribed to the medium acidic sites in the fresh catalyst. In the spent catalyst, the peak corresponding to the medium acidic site shifted to higher medium sites (~310 °C). This could be due to the blockage of pores by coking or water vapour in the spent samples, which took an extra effort to desorb the NH_3 molecules for the catalyst surface. The nature of acidic sites present on the catalyst surface was examined by pyridine-adsorbed FTIR, and the result is shown in Fig. 4b. The adsorption band at 1445, 1486, 1539, 1608, and 1634 cm^{-1} were

Table 2

Table 1
Product distribution from dehydration of bio-derived lactic acid over a different synthesised catalyst.

Entry	Catalysts	LA conv (%)	Product selectivity (%)				AA yield (%)
			AA	PA	AC	other	
1	20Na/Y	99.9	24.9	0	4.4	70.6	24.9
2	20Ca/Y	99.3	24.9	14.6	4.8	55	24.9
3	2Li20Na/Y	99.9	42.9	3.8	4.5	48.7	42.9
4	20Na/ZSM-5	99.8	51.7	4.2	3.8	40.1	51.7
5	2Li20Na/ZSM-5	99.8	54.3	1.4	5.9	38.2	54.3
6	MoP	60.4	47.5	1.2	4.5	7.2	28.6
7	MoS ₂	76.4	64.2	3.2	5.8	3.2	49.1
8	MoO ₃	96.7	19.3	71.3	4.6	1.3	18.6
9	Mo2P S	99.6	53.7	12.7	27.0	6.2	53.7
10	Mo2P S*	94.1	91.2	1.5	1	0.4	85.9
11	Mo4P S	98.3	49.0	8.4	26.3	14.6	49.0
12	Mo10P S	99.8	30.1	6.8	49.8	13.1	30.1
13	Mo15P S	97.9	44.6	39.3	0.2	14.1	44.6

Reaction condition: Catalyst weight – 1 gm(pelletised); Reaction temp: 400 °C; LHSV – 4h⁻¹ carrier gas –N₂, carrier gas flow –16 ml/ min; lactic acid conc.- 20%(w/W), TOS- 9 h⁻¹, other include acetic acid; 2,3 pentane dione and so on.

* 450 °C.

observed on MoP|S catalysts. The bands at 1634 and 1539 cm⁻¹ represent the Brønsted acid sites (BAS), the resultant after establishing pyridinium ions with proton sites [37]. The peak observed at 1486 cm⁻¹ is similar to Lewis and Brønsted acidic sites. The absorption bands of Lewis acid sites (LAS) appear at 1608 and 1445 cm⁻¹ [7]. It was believed that the Brønsted acidity might be due to H ion (from H₃PO₄), where the phosphorus is responsible for the Lewis acidity. Figure S7 exemplifies the ³¹P NMR spectrum of the Mo2P|S catalyst, and it displays a sharp, intense peak at 0 ppm chemical shift. It indicates the formation of the phosphate (PO₄³⁻) group (confirmed by XPS). The presence of other phosphoric acids can be omitted as the catalyst was calcined at 450 °C [38].

3.2. Performance test of various catalysts

The catalytic activities of all catalysts were tested in the vapour phase dehydration of biologically derived lactic acid (**Scheme 1**), and the results are given in **Table 2**. According to the literature, many combinations of MFI and FAU framework zeolites have been evaluated (entries 1–5). From the data, it can be seen that the reaction was attempted with basic and acidic metal moieties. Na- and Ca-based catalysts show similar AA yields among the basic metals. In addition, we added a catalyst amount of Li (2 wt%) to increase its basicity; the results with 2Li2ONa/Y show a passivation of the AA yield (entry 3). The same combination is attempted with MFI zeolites (i.e. ZSM-5, Si/Al-80), and the data (entry 5) show a substantial increase in AA yield compared to Y zeolite. After benchmarking the zeolite-based catalyst, we tried acidic MoP, MoS₂ and MoO₃-based catalysts but ended up with low AA yields in both cases (entries 6,7). Remarkably, the MoP|S-based catalyst outperformed all catalysts with 99.6% conversion and 53.7% selectivity (entry 9) at a temperature of 400 °C. At 450 °C, the catalyst shows 86.9%

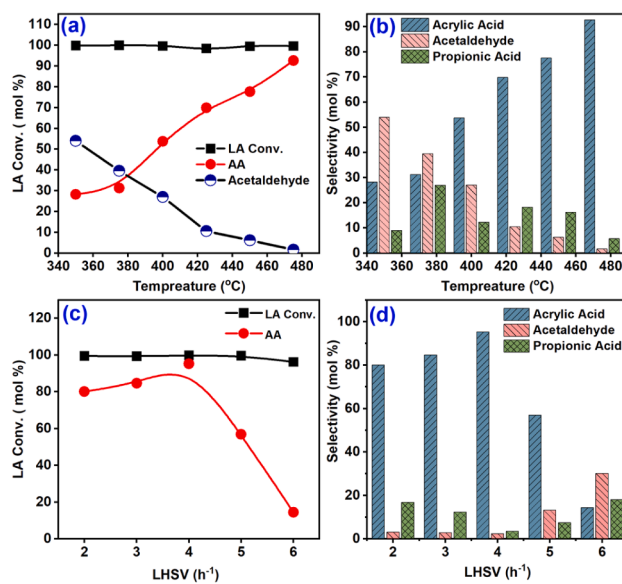


Fig. 6. Effect of temperature (a-b) and LHSV (c-d) on lactic acid (LA) conversion and product selectivity.

AA yield with 94.1% LA conversion. The gradually increased AA yield values for MoP|S, which imply the insertion of excess thiourea, created more edge and topological defects in the catalyst surface (discussed above). These abundant defect sites can modulate and tune the electronic and surface properties, thus optimising the activation energies of dehydration steps (discussed later) [39]. These performance indexes at entries 9–10 are comparable/better to those zeolites and some advanced metal-zeolite catalysts reported in the literature. Further increase in the phosphorous content (entry 11–13) does not really improve the AA yield, implicating the optimum phosphorous loading as 2 wt%.

The Mo2P/S catalyst was further tested in a temperature range from 350 to 475 °C (Fig. 6a, b), and a gradual increase in AA selectivity was observed. The selectivity of AA is 77.5%, achieving 99.5% lactic acid conversion at 450 °C. Considering the yield of AA at 450 °C reported in the literature; this is the maximum ever reported for a non-zeolite-based catalyst. At the same time, the selectivity of acetaldehyde (important among the by-products) decreased continuously (Fig. 6b). The maximum value of the acetaldehyde selectivity (54%) is reached at a temperature of 350 °C. Therefore, considering the inverse trend of acetaldehyde and AA selectivity, we can assume that the decarboxylation of LA is favoured at low temperatures (Scheme 1). The decarboxylation of LA is said to be mainly responsible for the low selectivity of acrylic acid at lower temperatures (Fig. 6b). In addition, the polymerisation of lactic acid becomes difficult due to incomplete gasification and leads to high selectivity to acetaldehyde.⁷ As the temperature further increased to 475 °C, the selectivity to acetaldehyde decreased to 1.6% while the selectivity to acrylic acid increased to 92.5%.

The progressive increase in LHSV from 2 to 6 h⁻¹ results in a reasonable decrease in LA conversion from 99.4 to 96.2%. This is due to the lack of contact time, although the decrease is nominal. Nevertheless, the selectivity of acrylic acid increases primarily through the LHSV from 2 to 4.0 h⁻¹ and then falls from 4.0 to 6.0 h⁻¹. The prolonged residence time at lower LHSV triggered secondary reactions, such as the decomposition of aa and other products, resulting in low aa selectivity [40]. On the other hand, short residence time leads to poor adsorption of the reactant, resulting in an induced non-catalytic thermal reaction for polymerisation from LA to coke [40]. At the same time, the selectivity for acetaldehyde (AC) gradually increases from 3 to 30.1%, with the LHSV increasing from 2 to 6 h⁻¹. Typically, the fermented broth contained ~ 20% lactic acid concentration, which was diluted and concentrated on studying the influence of feed concentration and the

Table 3

The rate equation for the elementary reactions.

Elementary steps	Rate Expression	Activation energy (kJ/mole)	Arrhenius Constant
Surface reaction	$RS = K \cdot PLA \cdot KM / (1 + PLA \cdot KM)$	18.56	2.39×10^{21}
Adsorption	$RA = K \cdot PLA$	16.09	1.84×10^{17}
Power law	$RLA = K(PLA)^m$	11.39	6.42×10^8

results are presented in Fig. 6. Increasing LA concentration showed a parabolic trend in conversion and aa selectivity. The maximum acrylic acid selectivity (88.4%) was reached at a lactic acid concentration of 20%. At low lactic acid concentrations, the rate of self-polymerisation of lactic acid leading to coke is slow [41]. At higher settings, the rate of self-polymerisation increases and causes additional coke deposition on the surface of the catalyst site, resulting in the deactivation of the catalytic site.

3.3. Kinetic study

The kinetic behaviour of catalyst Mo2P|S was shown as the partial pressure of lactic acid and as a function of temperature.

Rate of lactic acid consumption = (conversion of LA * flow rate of LA)/weight of catalyst used.

The expression is as follows:

$$-r_{LA} = Y_{LA} \cdot X_{LA} / W_{cat}$$

Here, -ve sign shows that lactic acid is consumed.

r_{LA} = rate of lactic acid (LA) consumption in $\mu\text{mol/g}$.

X_{LA} = fractional conversion of Lactic acid.

Y_{cat} = flow rate of lactic acid in ml/h changed to $\mu\text{mol/s}$.

W_{cat} = weight of catalyst in g.

In the kinetic tests, a set of experiments were carried out at different initial reactant concentrations, and the initial rates were calculated by differentiating the data. All the calculation was done under the kinetic regime at low conversion. The sample was collected after half an hour to ensure the stable performance of the catalyst. The rate and partial pressure are given in Table S2-S5; the experimental data were observed at four temperatures (400, 425, 450, 475) at an N₂ flow rate of 16 ml/min by varying flow rate of lactic acid. Firstly, the power law rate equation is supposed as

$$R_{LA} = K(P_{LA})^m$$

The order of the reaction at different temperatures was determined by a graph between lnR vs lnP plotted (Fig. 8a) to have R as the dependent variable and p as the independent variable. Similarly, we considered the elementary reaction steps as adsorption, surface reaction, and desorption by neglecting the diffusion processes, and all the kinetic calculation detailed in supporting information.

The Rcalculated from all the elementary steps has been evaluated in reference to the observed rate ($R_{observed}$) and shown in Fig. 9a-c. It is clear from the graph (from regression value) that the power law rate reaction is the best fit for the dehydration of lactic acid. Although, as the reaction proceeds through a heterogeneous catalyst, thus surface reaction step is also considered the rate-determined step. Further, the activation energy was calculated for the LA dehydration over Mo2P/S catalysed between 400 and 475 °C.

$$K = k_0 e^{(-E/RT)}$$

Arrhenius equation was plotted against the data set calculated for the power-law rate equation, adsorption, and surface reaction as rate-determining steps and shown in Fig. 8b-d. Calculating the equations, the Ea for the elementary reaction values is charted in Table 3.

The graph fitted to the experimental data is the surface rate-

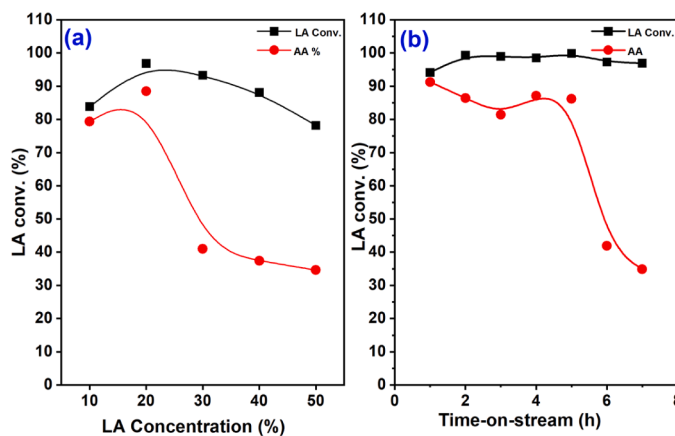


Fig. 7. Effect of lactic acid concentration on LA conversion and product selectivity.

determining step from these three equations. Hence, using the Arrhenius plot of the power law rate equation rate-determining mechanism, the activation energy for the reaction is found to be 11.39 KJ/mol.

3.4. Nature of carbon deposition and catalyst stability

The nature of coke deposition and change in the oxygen environment of the Mo-catalyst were elucidated by XP spectra shown in Fig. 10a. The deconvolution of the C 1 s spectrum of Mo₂P|S gives two peaks at 284.5 and 286.5 eV. The first peak is ascribed to the sp³-type graphitic, and the second peak is assigned to be C-O-C type carbon species [42,43]. The relative intensity of C-O-C in the spent Mo₂P|S catalyst seems to be low

compared to the fresh catalyst. However, the increase in the amount of graphitic coke is also noticed. The O1s spectra for all two samples (Fig. 10b) show a single peak at 530.3 eV, signifying the existence of metal oxide, an indenture with the Mo₃d [44]. The absence of peaks at 531.5 and 532.4 eV signifies no possible association of leaching as these peaks are attributed to oxides of phosphates and sulphates [45]. On the other hand, the O 1 s peak present adsorbed water was found to have a binding energy of 533.3 ± 0.3 eV [46]. In this study, the O1s spectra for the spent catalyst (Fig. 10b) show a single peak at 530.3 eV (described above), confirming the metal oxide. For a reaction with ~ 80% water-diluted feed, this implicates low or negligible water adsorption on the catalyst surface, inferring the catalyst's high-water tolerance. Further, the MoS₂ powder possessed a lamellar structure (Figure S1). Consequently, the XRD spectrum of MoP|S (Fig. 1) exhibited the peak at 12.8° for the (020) plane, where the space between adjacent layers was ~ 6.9 Å [47]. Therefore, it may be concluded that the MoP|S composite still showed a lamellar structure.

The stability of the catalyst was tested in terms of time-on-stream (TOS) at 450°C over Mo₂P|S (LHSV = 4 h⁻¹) with 20% lactic acid broth. A considerable change in the lactic acid conversion and acrylic acid selectivity is observed (Fig. 7b), and it was found that the conversion decreased from 99.3 to 94.3% after 9 h. When looking at the acrylic acid selectivity, it was stable till 5th h of the reaction. Then rapidly sagged and went < 10% at 8th h onward, inferring that the catalyst is stable up to 5 h.

4. Conclusions

This study represents a green approach for the bio-derived lactic acid to produce a high-value fine chemical, acrylic acid. The defects arise in MoP|S catalyst due to the increasing amount of thiourea creating

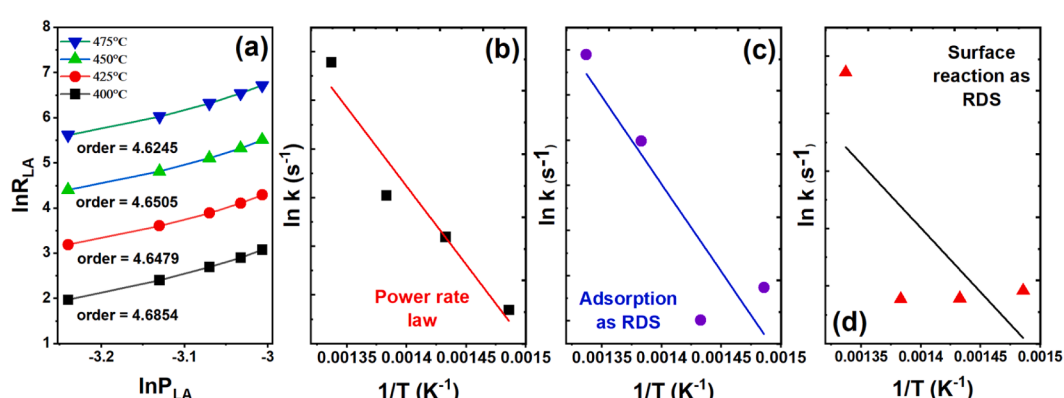


Fig. 8. (a) Plot between lnR(lactic acid) vs lnP(lactic acid) and (b-d) Arrhenius equation considering different elementary reaction steps.

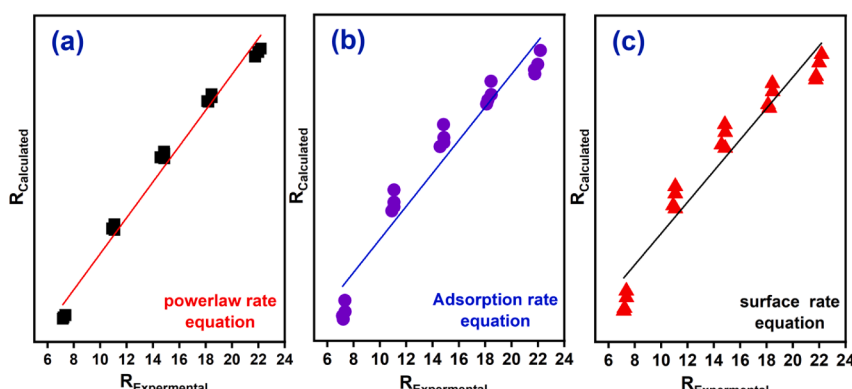


Fig. 9. The plot of R_{calculated} Vs R_{observed} of the data taken between 400 and 475 °C.

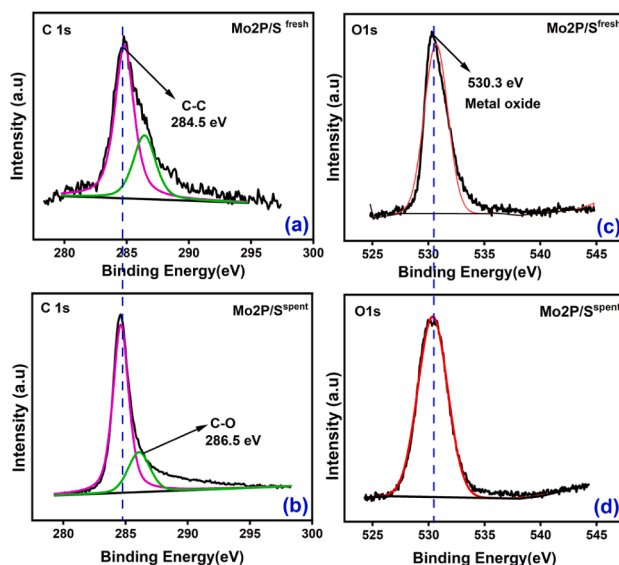


Fig. 10. XP spectra of C 1 s (a, c) and O 1 s (b, d) of spent and fresh Mo2P/S catalyst. N.B. the spent catalyst was recovered after 6 h time-on-stream.

additional active sites, leading to enhanced conversion and AA selectivity. Under optimised conditions, defect-rich Mo2P/S shows 94% LA conversion with 91% acrylic acid selectivity. The XPS data of O 1 s suggest low or negligible water adsorption, showing the catalyst's high-water tolerance. Kinetics study suggested that activation energy calculated using power law rate reaction is the best fit for the dehydration of lactic acid, and the activation energy (Ea) was found to be 11.39 kJ/mol. The catalyst performance discussed is better than those of zeolites and some advanced metal-zeolite catalysts reported in the literature. These findings should encourage researchers to synthesise catalysts with defects-rich edges and kinks for enhanced catalytic activity wherever the dehydration of lactic acid promises advantages over conventional production with a bio-based raw material source.

Declaration of Competing Interest

The authors declare that they have no known competing financial interests or personal relationships that could have appeared to influence the work reported in this paper.

Data availability

Data will be made available on request.

Acknowledgements

This work was supported by the Council of Scientific & Industrial Research (CSIR) New Delhi through Focused Based Research (CLP-FBR) (project no MLP-1169). N. D. thanks CSIR, New Delhi, India, for the Doctoral Fellowship. We also acknowledge the Director of CSIR-IIP and Dr Rajaram Bal for his kind support. The authors thank the Analytical Science Division and Nano-catalysis Area, CSIR-Indian Institute of Petroleum, for their analytical services.

Appendix A. Supplementary data

Supplementary data to this article can be found online at <https://doi.org/10.1016/j.cej.2023.143240>.

References

- [1] R. Goyal, O. Singh, A. Agrawal, C. Samanta, B. Sarkar, Advantages and limitations of catalytic oxidation with hydrogen peroxide: from bulk chemicals to lab scale process, *Catal. Rev.* (2020) 1–57.
- [2] A. Agrawal, N. Bansal, H. Raghav, A. Jana, R. Goyal, D. Ghosh, T. Bhaskar, B. Sarkar, Catalytic cracking of yeast-borne single-cell oil for the production of small-chain olefins over a PtSn/alumina catalyst, *Green Chem.* 25 (2023) 728–735.
- [3] O. Singh, A. Agrawal, N. Dhiman, B.P. Vempatapu, K. Chiang, S. Tripathi, B. Sarkar, Production of renewable aromatics from jatropha oil over multifunctional ZnCo/ZSM-5 catalysts, *Renew. Energy* 179 (2021) 2124–2135.
- [4] O. Singh, A. Agrawal, T. Selvaraj, I.K. Ghosh, B.P. Vempatapu, B. Viswanathan, R. Bal, B. Sarkar, Renewable Aromatics from Tree-Borne Oils over Zeolite Catalysts Promoted by Transition Metals, *ACS Appl. Mater. Interfaces* 12 (2020) 24756–24766.
- [5] O. Singh, T. Sharma, I. Ghosh, D. Dasgupta, B.P. Vempatapu, S. Hazra, A.L. Kustov, B. Sarkar, D. Ghosh, Converting Lignocellulosic Pentosan-Derived Yeast Single Cell Oil into Aromatics: Biomass to Bio-BTX, *ACS Sustain. Chem. Eng.* 7 (15) (2019) 13437–13445.
- [6] K. Abnett, EU countries approve landmark climate change law, *Reuters*, London, 2021.
- [7] R. Goyal, B.M. Abraham, O. Singh, S. Sameer, R. Bal, P. Mondal, One-pot transformation of glucose into hydroxymethyl furfural in water over Pd decorated acidic ZrO₂, *Renew. Energy* 183 (2022) 791–801.
- [8] P.T. Chazovachii, M.J. Somers, M.T. Robo, D.I. Collias, M.I. James, E.N.G. Marsh, P.M. Zimmerman, J.F. Alfaro, A.J. McNeil, Giving superabsorbent polymers a second life as pressure-sensitive adhesives, *Nat. Commun.* 12 (2021) 4524.
- [9] B. Sarkar, C. Pendem, L.N. Sivakumar Konathala, R. Tiwari, T. Sasaki, R. Bal, Cu nanoclusters supported on nanocrystalline SiO₂-MnO₂: a bifunctional catalyst for the one-step conversion of glycerol to acrylic acid, *Chem. Commun.* 50 (2014) 9707–9710.
- [10] R. Bal, B. Sarkar, R.K. Singha, C. Pendem, S.A. Shankha, S. Ghosh, Catalyst for single step conversion of glycerol to acrylic acid and process for the preparation thereof, Google Patents (2016).
- [11] S. James, Acrylic Acid Market Size, Share & Trend Analysis Report 2022, San Francisco, USA, 2016, pp. 120.
- [12] J. Hu, Z. Lu, H. Yin, W. Xue, A. Wang, L. Shen, S. Liu, Aldol condensation of acetic acid with formaldehyde to acrylic acid over SiO₂, SBA-15, and HZSM-5-supported V-P-O catalysts, *J. Ind. Eng. Chem.* 40 (2016) 145–151.
- [13] A. Wang, J. Hu, H. Yin, Z. Lu, W. Xue, L. Shen, S. Liu, Aldol condensation of acetic acid with formaldehyde to acrylic acid over Cs(Ce, Nd) VPO/SiO₂ catalyst, *RSC Adv.* 7 (76) (2017) 48475–48485.
- [14] A. Wang, C. Ye, D. Yu, Y. Ding, H. Yin, Synthesis of acrylic acid through aldol condensation of acetic acid with formaldehyde catalysed by Bi-, W- and Cs-doped B2O3/SiO₂ nanocomposites, *J. Chem. Technol. Biotechnol.* 97 (2022) 1665–1675.
- [15] Z. Guo, D.S. Theng, K.Y. Tang, L. Zhang, L. Huang, A. Borgna, C. Wang, Dehydration of lactic acid to acrylic acid over lanthanum phosphate catalysts: the role of Lewis acid sites, *PCCP* 18 (34) (2016) 23746–23754.
- [16] P. Mäki-Arvela, I.L. Simakova, T. Salmi, D.Y. Murzin, Production of Lactic Acid/Lactates from Biomass and Their Catalytic Transformations to Commodities, *Chem. Rev.* 114 (3) (2014) 1909–1971.
- [17] E. Blanco, P. Delichere, J.M.M. Millet, S. Loridant, Gas phase dehydration of lactic acid to acrylic acid over alkaline-earth phosphates catalysts, *Catal. Today* 226 (2014) 185–191.
- [18] J. Peng, X. Li, C. Tang, W. Bai, Barium sulphate catalysed dehydration of lactic acid to acrylic acid, *Green Chem.* 16 (2014) 108–111.
- [19] J. Zhang, Y. Zhao, M. Pan, X. Feng, W. Ji, C.-T. Au, Efficient Acrylic Acid Production through Bio Lactic Acid Dehydration over NaY Zeolite Modified by Alkali Phosphates, *ACS Catal.* 1 (1) (2011) 32–41.
- [20] B.O. Yan, L.-Z. Tao, Y.u. Liang, B.-Q. Xu, Sustainable Production of Acrylic Acid: Alkali-Ion Exchanged Beta Zeolite for Gas-Phase Dehydration of Lactic Acid, *ChemSusChem* 7 (6) (2014) 1568–1578.
- [21] H.F. Shi, Y.C. Hu, Y. Wang, H. Huang, KNaY-zeolite catalysed dehydration of methyl lactate, *Chin. Chem. Lett.* 18 (2007) 476–478.
- [22] J. Yan, D. Yu, H. Li, P. Sun, H.e. Huang, NaY zeolites modified by La³⁺ and Ba²⁺: the effect of synthesis details on surface structure and catalytic performance for lactic acid to acrylic acid, *J. Rare Earths* 28 (5) (2010) 803–806.
- [23] P. Baral, M. Munagala, Y. Shastri, V. Kumar, D. Agrawal, Cost reduction approaches for fermentable sugar production from sugarcane bagasse and its impact on techno-economics and the environment, *Cellul.* 28 (10) (2021) 6305–6322.
- [24] P. Baral, A. Pundir, V. Kumar, A.K. Kurmi, D. Agrawal, Expedited production of concentrated glucose-rich hydrolysate from sugarcane bagasse and its fermentation to lactic acid with high productivity, *Food Bioprod. Process.* 124 (2020) 72–81.
- [25] Z. Wu, J. Wang, K. Xia, W. Lei, X. Liu, D. Wang, MoS₂-MoP heterostructured nanosheets on polymer-derived carbon as an electrocatalyst for hydrogen evolution reaction, *J. Mater. Chem. A* 6 (2) (2018) 616–622.
- [26] J. Xie, H. Zhang, S. Li, R. Wang, X.u. Sun, M. Zhou, J. Zhou, X.W.D. Lou, Y.i. Xie, Defect-rich MoS₂ ultrathin nanosheets with additional active edge sites for enhanced electrocatalytic hydrogen evolution, *Adv. Mater.* 25 (40) (2013) 5807–5813.
- [27] É. Blanco, P. Afanasyev, G. Berhault, D. Uzio, S. Loridant, Resonance Raman spectroscopy as a probe of the crystallite size of MoS₂ nanoparticles, *C. R. Chim.* 19 (10) (2016) 1310–1314.
- [28] C. Stinner, R. Prins, T.h. Weber, Formation, Structure, and HDN Activity of Unsupported Molybdenum Phosphide, *J. Catal.* 191 (2) (2000) 438–444.

- [29] B. Sarkar, R. Goyal, L.N. Sivakumar Konathala, C. Pendem, T. Sasaki, R. Bal, MoO₃ Nanoclusters Decorated on TiO₂ Nanorods for Oxidative dehydrogenation of ethane to ethylene, *Appl Catal B* 217 (2017) 637–649.
- [30] S. Kumar Singh Patel, K. Dewangan, S. Kumar Srivastav, N. Kumar Verma, P. Jena, A. Kumar Singh, N. S. Gajbhiye, Synthesis of α -MoO₃ nanofibers for enhanced field-emission properties, *Advanced Mater. Lett.* 9 (8) (2018) 585–589.
- [31] S. Wang, J. Wang, P. Li, Z. Wu, X. Liu, N. P-Codoped Carbon Layer Coupled with MoP Nanoparticles as an Efficient Electrocatalyst for Hydrogen Evolution Reaction, *Materials* 11 (2018) 1316.
- [32] J. Miao, F.-X. Xiao, H.B. Yang, S.Y. Khoo, J. Chen, Z. Fan, Y.-Y. Hsu, H.M. Chen, H. Zhang, B. Liu, Hierarchical Ni-Mo-S nanosheets on carbon fiber cloth: A flexible electrode for efficient hydrogen generation in neutral electrolyte, *Sci. Adv.* 1 (2015) e1500259.
- [33] L. Chai, W. Yuan, X. Cui, H. Jiang, J. Tang, X. Guo, Surface engineering-modulated porous N-doped rod-like molybdenum phosphide catalysts: towards high activity and stability for hydrogen evolution reaction over a wide pH range, *RSC Adv.* 8 (2018) 26871–26879.
- [34] Y. Huang, Y. Sun, X. Zheng, T. Aoki, B. Pattengale, J. Huang, X. He, W. Bian, S. Younan, N. Williams, Atomically engineering activation sites onto metallic 1T-MoS₂ catalysts for enhanced electrochemical hydrogen evolution, *Nat. Commun.* 10 (2019) 982.
- [35] B. Lassalle-Kaiser, D. Merki, H. Vrubel, S. Gul, V.K. Yachandra, X. Hu, J. Yano, Evidence from *in situ* X-ray absorption spectroscopy for the involvement of terminal disulfide in the reduction of protons by an amorphous molybdenum sulfide electrocatalyst, *J. Am. Chem. Soc.* 137 (2015) 314–321.
- [36] S. Macis, J. Rezvani, I. Davoli, G. Cibin, B. Spataro, J. Scifo, L. Faillace, A. Marcelli, Structural evolution of MoO₃ thin films deposited on copper substrates upon annealing: an X-ray absorption spectroscopy study, *Condens. Matter* 4 (2019) 41.
- [37] P.P. Upare, J.-W. Yoon, M.Y. Kim, H.-Y. Kang, D.W. Hwang, Y.K. Hwang, H. H. Kung, J.-S. Chang, Chemical conversion of biomass-derived hexose sugars to levulinic acid over sulfonic acid-functionalised graphene oxide catalysts, *Green Chem.* 15 (2013) 2935–2943.
- [38] T. Okuhara, T. Nishimura, M. Misono, Novel microporous solid “Superacids”: Cs_xH_{3-x}PW₁₂O₄₀ (2 ≤ x ≤ 3), in: J.W. Hightower, W. Nicholas Delgass, E. Iglesia, A.T. Bell (Eds.), *Studies in Surface Science and Catalysis*, Elsevier, 1996, pp. 581–590.
- [39] H. Jiang, J. Gu, X. Zheng, M. Liu, X. Qiu, L. Wang, W. Li, Z. Chen, X. Ji, J. Li, Defect-rich and ultrathin N doped carbon nanosheets as advanced trifunctional metal-free electrocatalysts for the ORR, OER and HER, *Energ. Environ. Sci.* 12 (2019) 322–333.
- [40] B. Yan, L.-Z. Tao, Y. Liang, B.-Q. Xu, Sustainable production of acrylic acid: catalytic performance of hydroxyapatites for gas-phase dehydration of lactic acid, *ACS Catal.* 4 (2014) 1931–1943.
- [41] V.C. Ghantati, S.T. Lomate, M.K. Dongare, S.B. Umbarkar, Catalytic dehydration of lactic acid to acrylic acid using calcium hydroxyapatite catalysts, *Green Chem.* 15 (2013) 1211–1217.
- [42] B. Sarkar, R. Goyal, C. Pendem, T. Sasaki, R. Bal, Highly nanodispersed Gd-doped Ni/ZSM-5 catalyst for enhanced carbon-resistant dry reforming of methane, *J. Mol. Catal. A Chem.* 424 (2016) 17–26.
- [43] A. Dolgov, D. Lopaev, C.J. Lee, E. Zoethout, V. Medvedev, O. Yakushev, F. Bijkerk, Characterisation of carbon contamination under ion and hot atom bombardment in a tin-plasma extreme ultraviolet light source, *Appl. Surf. Sci.* 353 (2015) 708–713.
- [44] J. Gomez-Bolivar, I.P. Mikheenko, R.L. Orozco, S. Sharma, D. Banerjee, M. Walker, R.A. Hand, M.L. Merroun, L.E. Macaskie, Synthesis of Pd/Ru bimetallic nanoparticles by *Escherichia coli* and potential as a catalyst for upgrading 5-hydroxymethyl furfural into liquid fuel precursors, *Front. Microbiol.* 10 (2019) 1276.
- [45] C.D. Wagner, *Handbook of x-ray photoelectron spectroscopy: a reference book of standard data for use in x-ray photoelectron spectroscopy*, Perkin-Elmer 1979.
- [46] A.P. Grosvenor, B.A. Kobe, N.S. McIntyre, Studies of the oxidation of iron by water vapour using X-ray photoelectron spectroscopy and QUASESTTM, *Surf. Sci.* 572 (2004) 217–227.
- [47] X. Zhang, L. Lin, T. Zhang, H. Liu, X. Zhang, Catalytic dehydration of lactic acid to acrylic acid over modified ZSM-5 catalysts, *Chem. Eng. J.* 284 (2016) 934–941.